coatings

MDPI

Article

From Mine Waste to Road Base: Cracking Resistance and Durability of Cement-Stabilized Crushed Stone Incorporating Lead–Zinc Mine Waste Rock Aggregate

Yinglong Hu [1], Chenghai Sun [1], Lizhou Zhao [1], Zhengwei Zhang [2,*], Jian Miao [3], Jinggang Yin [3] and Xiang Liu [4,5,*]

[1] Yunnan Yunlan Expressway Investment and Development Co., Ltd., Pumi Autonomous County 671400, China
[2] School of Civil Aviation, Xihang University, Xi'an 710077, China
[3] YCIH Road Surface Engineering Co., Ltd., Kunming 650501, China
[4] Faculty of Transportation Engineering, Kunming University of Science and Technology, Kunming 650500, China
[5] Yunnan Science & Technology Research Institute of Highway, Kunming 650051, China
* Correspondence: z.zhengwei@xaau.edu.cn (Z.Z.); lx@kust.edu.cn (X.L.)

Highlights

What are the main findings?

- A 50% coarse aggregate replacement with lead-zinc mine waste rock was feasible in cement-stabilized crushed stone under the investigated laboratory conditions.
- A 4‰ basalt fiber dosage demonstrated enhanced cracking and scouring resistance among the investigated dosages.
- The sulfate-resistant agent reduced mass loss and improved strength retention under sulfate wet–dry cycling.

What are the implications of the main findings?

- The results preliminarily support the use of mine waste rock as a partial substitute for natural coarse aggregate in road base materials.
- Basalt fiber provides a potential modification strategy for improving cracking resistance and durability.
- Long-term exposure, environmental stability, heavy metal release, and field performance require further investigation before broad engineering application.

Abstract

To alleviate the shortage of high-quality natural aggregates and promote the sustainable utilization of mining waste rock, this study employed lead–zinc mine waste rock-derived aggregate to replace 50% of the coarse aggregate by mass in cement-stabilized crushed stone. A series of tests, including drying shrinkage, thermal shrinkage, freeze–thaw cycling, scouring, and sulfate attack, were conducted to investigate the cracking resistance and durability of the resulting mixtures. The effects of basalt fiber, low-alkali cement, and a sulfate-resistant agent were further evaluated. Although the waste rock aggregates exhibited relatively inferior particle morphology, they could be incorporated into cement-stabilized crushed stone through rational gradation design. Among the investigated fiber contents, the mixture containing 4‰ basalt fiber exhibited relatively favorable shrinkage, freeze–thaw, and scouring resistance. The sulfate-resistant agent reduced mass loss and strength degradation under the investigated sulfate wet–dry cycling conditions. In contrast, low-alkali cement showed limited effectiveness in improving shrinkage resistance and freeze–thaw durability. These results provide experimental evidence for the feasibility of

Check for updates

Academic Editor: Paolo Castaldo

Received: 11 June 2026
Revised: 5 August 2026
Accepted: 6 August 2026
Published: 12 August 2026

Copyright: © 2026 by the authors. Licensee MDPI, Basel, Switzerland. This article is an open access article distributed under the terms and conditions of the Creative Commons Attribution (CC BY) license.

using lead–zinc mine waste rock as a partial coarse aggregate replacement in road base materials under the investigated laboratory conditions.

Keywords: lead–zinc mine waste rock; sustainable utilization of mine waste; cement-stabilized crushed stone; cracking resistance; durability

1. Introduction

Cement-stabilized crushed stone is widely used as a semi-rigid base or subbase material and occupies a dominant position in high-grade highway pavement structures in China because of its high load-bearing capacity and strong resistance to deformation [1]. However, its extensive application relies heavily on high-quality natural aggregates, such as basalt, diabase, and limestone [2,3]. In many regions, particularly mountainous plateau areas such as Yunnan Province, the increasing scarcity of conventional aggregates, long transportation distances, excessive quarrying, and ecological protection constraints have become major factors restricting infrastructure construction and sustainable development. As the supply of high-quality aggregates becomes increasingly limited and the environmental pressure associated with quarrying intensifies, the development of environmentally friendly and economically viable alternative aggregates has become an important research direction in highway engineering [4,5].

Meanwhile, the enormous quantities of solid waste generated by mining activities, particularly mine waste rock and tailings, impose a substantial environmental burden. In recent years, one major pathway for the resource utilization of mine waste rock worldwide has been its use as an alternative raw material in the production of cement, ceramics, concrete, bricks, and other construction materials. In Morocco, several studies have investigated the use of phosphate mine waste rock from the Benguerir mining area as an alternative aggregate in concrete [6], an embankment fill material [7], and a constituent of cement mortar [8], as well as the use of copper mine waste rock from the Blieda mining area as a substitute for natural sand [9]. Phosphate mine waste rock has also been combined with phosphate washing sludge to produce compressed stabilized earth bricks [10]. Moreover, alkali activation of phosphate mine waste rock using different alkaline activator solutions has been reported to produce materials with relatively high load-bearing capacity [11]. In India, more than 500 million tonnes of industrial waste, mining waste, and tailings are generated annually, and these materials have been identified as potential secondary raw materials for the production of cement, bricks, concrete, panels, and other construction materials, as well as for broader infrastructure development [12]. Other studies have similarly demonstrated the potential of iron ore waste rock and coal mining waste for the production of concrete, ceramics, and related materials [13,14].

Another major resource utilization pathway involves the use of mine waste rock as a filling material in mined-out voids, embankments, and other engineering applications. A method has been proposed for preparing cemented tailings–waste-rock powder backfill by combining mine waste rock with tailings [15]. At the Jinchuan nickel mine, a series of low-cost backfill mining technologies have been developed using solid wastes, including the replacement of cement with metallurgical slag to produce low-cost cementitious binders, the use of waste rock combined with rod-mill sand or tailings as mixed aggregates, and the incorporation of fly ash or copper beneficiation tailings into mixed aggregate systems [16]. A study on mine waste rock and tailing sand from the Kangjiawan lead–zinc–gold–silver mine showed that tailing sand could be used to backfill underground mined-out areas,

whereas waste rock and part of the tailing sand could be utilized in the production of construction materials [17].

In addition, a limited number of studies have explored the application of mine waste rock and tailings in road engineering. In the Democratic Republic of the Congo, coltan mine waste rock was reported to exhibit cohesive-soil characteristics but relatively poor road performance. Nevertheless, when incorporated at a proportion of 60% in a stabilized mixture, the resulting material generally satisfied the essential performance requirements for pavement subbases [18]. In Iran, two types of stripping waste from the Golgohar iron mine were found to be suitable for use in cement-stabilized crushed-stone bases after stabilization treatment [19]. A feasibility study of mine stripping materials from the Wuhai mining area in Inner Mongolia, China, showed that the materials exhibited relatively low frost-heave susceptibility and could be used as subgrade fill in seasonally frozen regions. The study further recommended maintaining a coarse-particle content of 40%–60% to improve the environmental adaptability of the subgrade under seasonal freezing conditions [20].

Lead and zinc are among the most extensively mined nonferrous metal resources. Previous studies have reported an average tailings generation coefficient of approximately 3.6, indicating that approximately 3.6 tonnes of tailings are generated for every tonne of concentrate produced [21,22]. Lead–zinc mining also generates large quantities of mine waste rock. The long-term accumulation of these wastes not only occupies substantial land resources but also poses serious threats to the surrounding atmosphere, soil, surface water, and broader ecological environment [23]. Lead–zinc mine waste rock and tailings are commonly processed into fine aggregates, sand, or fillers for the production of concrete, fired bricks, and unfired bricks, or mixed with cementitious slurry for backfilling mined-out voids. A study conducted at the Hazine Mağara mining area in Türkiye investigated concrete prepared by replacing limestone with lead–zinc mine waste rock at levels of 25%, 50%, and 75%. The resulting specimens exhibited reduced porosity and water absorption and increased density, which contributed to improvements in compressive and tensile strength [24]. Another study found that replacing conventional dolomite with lead–zinc mine waste rock at proportions not exceeding 40% produced no evident adverse effects on either the sintering process or the quality of the resulting sinter [25].

Nevertheless, studies directly applying lead–zinc mine waste rock in cement-stabilized crushed-stone bases remain limited. In terms of cracking resistance, the inherent drying and thermal shrinkage characteristics of cement-stabilized crushed stone can readily induce cracking. Moreover, mine waste rock used as coarse aggregate may exhibit relatively low intrinsic strength and unfavorable particle morphology, potentially resulting in insufficient scouring resistance and poor freeze–thaw durability and thereby increasing the risk of shrinkage cracking during service. Owing to the distinctive physical characteristics of mine waste rock aggregates, such as potentially high fine-particle contents and complex pore structures, as well as their chemical characteristics, including the possible presence of sulfur-bearing compounds, these materials may undergo deterioration mechanisms under aggressive environments that differ from those of conventional aggregates [26].

It is also noteworthy that national policies in China are actively promoting the resource utilization of bulk solid waste. The Guiding Catalogue for Industrial Restructuring (2024 Edition), issued in 2023, explicitly encourages the environmentally responsible production of sand and gravel aggregates from bulk wastes, including tailings, construction waste, industrial residues, municipal sludge, and sediments from rivers, lakes, channels, and marine environments [27]. Yunnan Province is an important lead–zinc mining region in China, and the Jinding lead–zinc mining area in western Yunnan contains enormous quantities of waste rock and tailings that have not yet been effectively utilized. High-quality limestone

aggregate sources are located far from the expressway projects in this region, whereas the waste rock stockpiles distributed around the Jinding mining area represent a potentially valuable source of road construction materials. Against this background, developing lead–zinc mine waste rock as a road aggregate is consistent with the engineering principles of adapting measures to local conditions and utilizing locally available materials. Such an approach could alleviate regional shortages of high-quality aggregates, consume substantial quantities of mining waste, reduce environmental pressures, and promote coordination between infrastructure construction and mine environmental management. It therefore has important practical implications for advancing low-impact highway development and contributing to China's carbon-peaking and carbon-neutrality goals.

Accordingly, to promote the high-value utilization of lead–zinc mine waste rock and evaluate its engineering applicability, this study investigated its use as a partial alternative aggregate in cement-stabilized crushed stone. Drying and thermal shrinkage tests were first conducted to characterize the cracking resistance of cement-stabilized crushed stone incorporating lead–zinc mine waste rock aggregate. Freeze–thaw cycling, scouring, and sulfate attack tests were subsequently performed to evaluate its durability. Specifically, freeze–thaw testing was used to simulate deterioration under cyclic temperature variations in cold environments and to assess frost resistance and strength loss. Scouring tests were conducted to evaluate material stability under hydraulic impact by examining particle loss and surface deterioration. Sulfate attack testing was used to quantify mass loss and mechanical performance degradation under an aggressive sulfate environment. The effects of basalt fiber, low-alkali cement, and a sulfate-resistant agent were also evaluated as representative modification strategies. Overall, this study provides an experimental basis for the broader utilization of lead–zinc mine waste rock in road base materials and supports the coordinated development of mining-waste management and sustainable transportation infrastructure in Yunnan Province.

2. Materials and Methods

2.1. Raw Materials

2.1.1. Lead–Zinc Mine Waste Rock Aggregate

The Jinding mining area, located in Lanping County, Yunnan Province, hosts one of the major large-scale lead–zinc deposits in China and contains substantial quantities of low-grade complex oxidized lead–zinc ores. More than 80% of the mining operations are conducted using open-pit methods. To expose and extract the buried ore bodies, non-ore or low-grade rock strata overlying and surrounding the ore bodies must first be stripped, thereby generating large quantities of mine waste rock. During the 2025–2026 open-pit stripping project, approximately 15.4285 million m^3 of material was stripped, whereas only approximately 0.50 million m^3 of by-product ore was recovered, indicating that the quantity of waste rock generated was substantially greater than the ore output. Together with the accumulated low-grade ore stockpiles, the total quantity of waste rock and low-grade ore residues in the mining area has reached the hundred-million-tonne scale. The lead–zinc mine waste rock used in this study was collected from this mining area. The technical procedure from waste-rock selection to aggregate processing and preparation is illustrated in Figure 1.



Figure 1. Technical process for sampling, processing, and preparation of lead–zinc mine waste rock aggregate.

Due to the large distribution area of the waste rock accumulation site, unmanned aerial vehicle reconnaissance was first conducted to determine representative sampling regions. Based on visual characteristics, weathering degree, and empirical judgments such as hammer impact observations, ten representative areas were initially selected for waste rock sampling.

After crushing and screening, the processed waste rock aggregates exhibited two typical appearances, namely yellowish-brown and bluish-black particles. Based on manual separation and mass statistics, the average mass ratio of yellowish-brown to bluish-black aggregates was approximately 4:6. Considering the difficulty of separating different types of waste rock during practical production, the waste rock aggregates used in subsequent laboratory experiments were prepared according to this ratio, which may better represent the distribution characteristics of the waste rock in the field. For concise presentation, yellow-brown waste rock aggregate (YWR), bluish-black waste rock aggregate (BWR), and mixed waste rock aggregate (MWR) are used hereafter.

(1) Properties of Coarse Aggregate

The coarse aggregates used in the cement-stabilized crushed stone consisted of MWR and limestone. The relevant properties were tested in accordance with the Test Methods of Aggregates for Highway Engineering (JTG 3432-2024) [28], while the specification limits were taken from JTG F40 [29]. The results are presented in Table 1.

All measured indices of the waste rock coarse aggregates satisfied the applicable specification requirements. However, the crushing value and flakiness and elongation indices of the waste rock aggregates were relatively high. Compared with the limestone coarse aggregate produced using the same crushing and screening equipment and process, the waste rock aggregates exhibited relatively inferior particle morphology and strength, which may be associated with their intrinsic lithological characteristics.

Table 1. Technical properties of coarse aggregates.

Technology Index	Unit	Expressways		Method	YWR	BWR	MWR	Limestone
		Surface	Other					
Crushing Value of Aggregate	%	≤26	≤28	T 0316	21.46	24.1	23.75	16.8
Los Angeles Abrasion Loss	%	≤28	≤30	T 0317	10.13	11.94	12.3	10.5
Apparent Relative Density	-	≥2.60	≥2.50	T 0304	2.68	2.74	2.71	2.7
Water Absorption	%	≤2.0	≤3.0	T 0304	0.47	0.45	0.47	0.43
Soundness	%	≤12	≤12	T 0314	3	2.3	2.6	2.8
Flakiness & Elongation >9.5 mm	%	≤12	≤15	T 0312	11.7	11.1	11.78	2.3
Flakiness & Elongation ≤9.5 mm	%	≤18	≤20	T 0312	15.1	14.6	14.6	2.9
<0.075 mm (Washing Method)	%	≤1	≤1	T 0310	0.19	0.26	0.23	0.8
Soft Particle Content	%	≤3	≤5	T 0320	2.49	2	2.3	1.2

(2) Properties of Fine Aggregates

Fine aggregates play a crucial role in the mixture, as they not only fill the voids between coarse aggregates to enhance mixture compactness but also influence the overall in-service performance of the pavement. The fine aggregates used in cement-stabilized crushed stone are composed of limestone. Conformity tests for key indices of the fine aggregates were conducted in strict accordance with the technical requirements specified in the Test Methods of Aggregates for Highway Engineering (JTG 3432-2024). The results are presented in Table 2. All indicators conform to the requirements of the specification.

Table 2. Technical properties of limestone fine aggregate.

Technology Index	Unit	Expressway	Test Method	Limestone
Apparent Relative Density	-	≥2.5	T 0328	2.73
Particle Content < 0.075 mm	%	≤3	T 0333	1.2
Sand Equivalent	%	≥60	T 0334	73
Methylene Blue Value	g/kg	≤25	T 0349	1
Angularity (Flow Time)	s	≥30	T 0345	59.1

2.1.2. Cement

Cement is the principal binder in cement-stabilized crushed stone, providing cohesion among aggregate particles and forming a mechanically stable structure after hydration.

(1) Reference Portland cement

Huaxin Portland cement (Huaxin Cement Co., Ltd., Wuhan, China) with a strength grade of 42.5 was selected as the reference Portland cement. Its technical properties were tested according to the Test Methods of Cement and Concrete for Highway Engineering (JTG 3420-2020) [30]. The requirements were referenced from Common Portland Cement (GB 175-2023) [31] and the Technical Guidelines for Construction of Highway Pavement Base Courses (JTG/T F20-2015) [32]. The results are presented in Table 3, and all measured properties satisfied the relevant requirements.

Table 3. Technical properties of the reference Portland cement.

Technology Index	Unit	Requirement	Measured Value	Test Method
Fineness	%	≤10	8	T 0502-2005
Initial setting time	min	≥45	52	T 0505-2020
Final setting time	h	≤10	6	T 0505-2020
Volumetric stability	/	≤5.0 mm	qualified	T 0505-2020

Table 3. *Cont.*

Technology Index	Unit	Requirement		Measured Value	Test Method
Compressive Strength	MPa	3 d	≥21.0	24.1	T 0506-2005
		28 d	≥42.5	43.1	T 0506-2005
Flexural Strength	MPa	3 d	≥4.0	5	T 0506-2005
		28 d	≥6.5	8.1	T 0506-2005

(2) Low-Alkali Cement

The low-alkali cements used in this study were produced by Dali Hongshi Cement Co., Ltd., (Dali, China). According to JTG/T F20-2015, Portland cements with strength grades of 32.5 and 42.5 may be used in cement-stabilized base materials. In practice, the appropriate strength grade depends on the aggregate properties, mixture proportion, and required mechanical performance. Therefore, two low-alkali ordinary Portland cement (P.O.) grades, P.O. 32.5 and P.O. 42.5, were investigated to evaluate their effects on cracking resistance and durability. The available technical properties are summarized in Table 4.

Table 4. Technical properties of P.O. 32.5 and P.O. 42.5 low-alkali cements.

Technology Index	Unit	P.O. 32.5			P.O. 42.5			Test Method
		Requirement		Measured	Requirement		Measured	
Fineness	%	≤30		13.2	≤10		1.5	T 0502-2005
Initial setting time	min	≥45		52	≥45		50	T 0505-2020
Final setting time	h	≤10		4.0	≤10		4.08	T 0505-2020
Volumetric stability	/	boiling test qualified		qualified	≤5.0 mm		qualified	T 0505-2020
Compressive strength	MPa	3 d	≥12.0	14.5	3 d	≥21.0	28.0	T 0506-2005
		28 d	≥32.5	38.2	28 d	≥42.5	42.5	T 0506-2005
Flexural strength	MPa	3 d	≥3.5	4.1	3 d	≥4.0	4.9	T 0506-2005
		28 d	≥5.0	5.7	28 d	≥6.5	7.1	T 0506-2005

2.1.3. Additives

Three modification strategies were investigated: low-alkali cement, basalt fiber, and a sulfate-resistant agent. Their effects on the cracking resistance and durability of waste rock aggregate cement-stabilized crushed stone were evaluated.

(1) Basalt Fiber

Chopped basalt fiber with a nominal length of 12 mm, produced by Changsha Ningxiang Building Materials Co., Ltd., (Changsha, China), was used. Basalt fiber was selected because of its high tensile strength, chemical stability, and compatibility with cementitious materials. Fiber bridging may restrain crack initiation and propagation and thereby improve the shrinkage resistance and durability of cement-based materials. The technical parameters are presented in Table 5.

Table 5. Technical parameters of basalt fiber.

Density	Operating Temperature	Tensile Strength	Elastic Modulus	Ultimate Elongation	Alkali Resistance Retention Rate	Hygroscopicity
g/cm^3	°C	Mpa	Gpa	%	%	
2.62	369–770	1938	76.1	2.9	75	<0.1

(2) Sulfate-Resistant Agent

An SK-D sulfate-resistant agent (SK-D is the manufacturer's product designation) produced by Qingdao Zhuoneng Construction Technology Co., Ltd., (Qingdao, China), was used to improve the sulfate attack resistance of the cement-stabilized crushed stone. The agent is intended to reduce expansion-related deterioration and improve durability under sulfate exposure. Its technical properties are listed in Table 6.

Table 6. Technical properties of the SK-D sulfate-resistant agent.

Technology Index	Unit	Requirement	Measured Value	Test Method
Initial setting time	min	≥45	120	JC/T 1011-2021
Final setting time	h	≤10	8.5	JC/T 1011-2021
Expansion ratio	%	1 d ≥0.05	0.08	JC/T 1011-2021
		28 d ≤0.60	0.39	JC/T 1011-2021
Erosion resistance coefficient K	/	≥0.90	0.93	JC/T 1011-2021
Expansion coefficient E	/	≤1.50	1.32	JC/T 1011-2021
Chloride diffusion coefficient ratio, 28 d	/	≤0.85	0.74	JC/T 1011-2021
compressive strength ratio	%	3 d ≥90	96	JC/T 1011-2021
		28 d ≥100	105	JC/T 1011-2021

2.2. Mixture Design

Based on previous studies [33] and the C-B-3 gradation limits specified in JTG/T F20-2015, the aggregate gradation adopted in this study was determined. The corresponding gradation curve is presented in Figure 2.

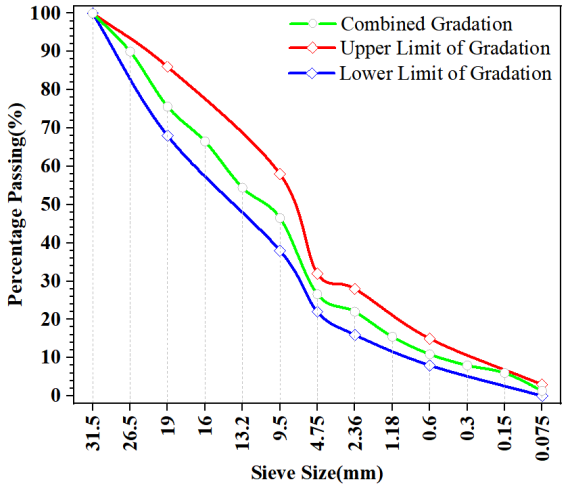


Figure 2. Aggregate gradation curve.

The waste rock aggregate accounted for 50% of the total mass of the coarse aggregate fraction. This replacement level was selected by considering the engineering feasibility of maintaining a stable aggregate skeleton and the objective of increasing the utilization of mine waste rock. It represents a moderate replacement level for evaluating the mixture under practical laboratory conditions and should not be interpreted as an optimized replacement ratio.

The heavy compaction method was used to determine the optimum moisture content and maximum dry density. The compaction curve is shown in Figure 3. The cement content was defined as the ratio of cement mass to the total mass of dry aggregates and was set

at 4%. The corresponding maximum dry density and optimum moisture content were 2.32 g/cm^3 and 5.2%, respectively. All subsequent specimens were prepared using this basic mixture proportion.

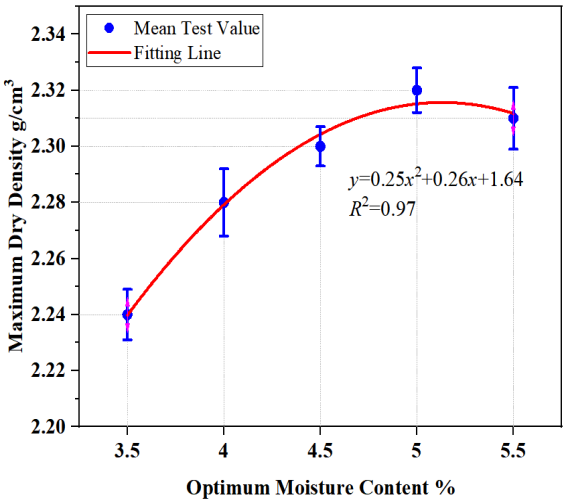


Figure 3. Compaction curve at 4% cement content.

The basalt fiber content was defined as the mass ratio of basalt fiber to the total aggregate mass. Fiber contents of 0‰, 2‰, 4‰, and 6‰ were investigated, with the 0‰ mixture serving as the control. The three nonzero levels were selected to represent relatively low, moderate, and relatively high fiber contents and to evaluate the influence of fiber dosage on cracking resistance and durability.

2.3. Cracking Resistance and Durability Tests

2.3.1. Drying Shrinkage Test

The drying shrinkage performance of waste rock aggregate cement-stabilized crushed stone was evaluated according to Method T 0576-2020 in the Test Methods of Cement and Concrete for Highway Engineering (JTG 3420-2020). Beam specimens with dimensions of 100 mm × 100 mm × 400 mm were prepared following Method T 0551, with three specimens per group and two groups for each mixture. One group was used to measure drying shrinkage deformation, and the other was used to determine water loss. All specimens were cured under standard conditions for 7 days at 20 °C and 95% relative humidity. During the first 7 days of testing, dial-gauge readings were recorded daily at fixed intervals, and the reference specimens were weighed simultaneously. From day 7 to day 31, measurements were recorded every 2 days, with additional measurements on days 60 and 90. After completion of the shrinkage measurements, the reference specimens were oven-dried to constant mass to determine their final moisture condition. The testing process is illustrated in Figure 4, and the results were calculated according to Method T 0576-2020.

2.3.2. Temperature Shrinkage Test

The thermal shrinkage performance of waste rock aggregate cement-stabilized crushed stone was evaluated according to Method T 0855-2024 in the Test Methods of Materials Stabilized with Inorganic Binders for Highway Engineering (JTG 3441-2024) [34]. Beam specimens with dimensions of 100 mm × 100 mm × 400 mm were prepared following Method T 0551. All specimens were cured under standard conditions for 7 days and then oven-dried at 105 °C. During testing, each specimen was placed vertically in the instrument chamber, and a displacement sensor was installed. Appropriate preloading was applied to

adjust the sensor reading to the middle of its measurement range. The testing process is illustrated in Figure 5.



Figure 4. Drying shrinkage test procedure.



Figure 5. Thermal shrinkage test procedure.

Considering the climatic characteristics of Yunnan, six temperature control points were established from 40 °C to −10 °C at intervals of 10 °C. Cooling between adjacent temperature points lasted 30 min, and each temperature was maintained for 2 h. The thermal shrinkage strain and thermal shrinkage coefficient were used as the principal evaluation indices.

2.3.3. Freeze–Thaw Cycling Test

The freeze–thaw resistance of waste rock aggregate cement-stabilized crushed stone was evaluated according to Method T 0858-2009 in JTG 3441-2024. A total of 24 cylindrical specimens, 150 mm in diameter and 150 mm in height, were prepared according to Method T 0845. At each curing age of 28, 60, 90, and 180 days, three specimens were assigned to the control group and three to the freeze–thaw group. Thus, each condition at each curing age contained three replicate specimens. When the designated curing age was reached, the control specimens were surface-dried, their dimensions and masses were recorded, and their unconfined compressive strengths were measured.

For the freeze–thaw group, specimens were placed in a low-temperature chamber at −18 °C for 16 h, as illustrated in Figure 6. After removal, their dimensions and masses

were measured, and the specimens were immediately transferred to a water bath at 20 °C for 8 h. After surface moisture was removed, the dimensions and masses were measured again. This procedure constituted one freeze–thaw cycle. Five cycles were applied, after which unconfined compressive strength was measured, as shown in Figure 7. Freeze–thaw resistance was evaluated using the strength before and after cycling and the freeze–thaw resistance coefficient.



Figure 6. Freeze–thaw cycling process.



Figure 7. Freeze–thaw resistance test.

2.3.4. Erosion Resistance Test

A scouring test system was constructed according to the apparatus and principles described in the literature [35]. The system consisted mainly of a water tank, scouring platform, hoses, booster pump, and spray nozzle, as illustrated in Figure 8. A plastic tank measuring approximately 107 cm × 107 cm × 76 cm, with a capacity of 700 L, served as the main test area. A scouring platform was installed at the center, and three fixing blocks were used to secure the specimen. A metal spray nozzle was installed at an appropriate

distance above the platform and connected by hose to a booster pump and water reservoir to provide a stable water supply.

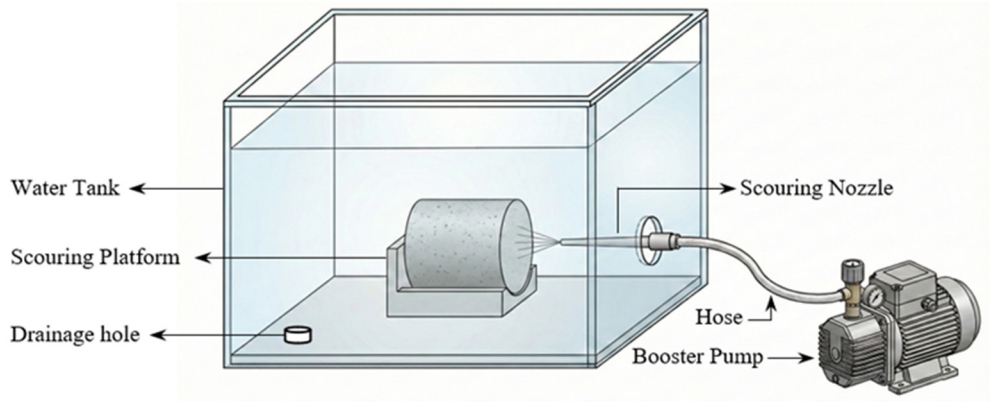


Figure 8. Schematic diagram of the scouring test system.

Cylindrical specimens, 150 mm in diameter and 150 mm in height, were prepared according to Method T 0845. Eight groups with three replicate specimens per group were cured for 28, 60, 90, and 180 days, with two groups assigned to each curing age. The test procedure followed Ref. [30]. The nozzle rotation speed was 1 Hz, and the booster-pump outlet pressure was maintained at 140 kPa, corresponding to the estimated pore-water pressure in a base layer under a standard axle load of 100 kN at a vehicle speed of 60 km/h. Scouring was terminated after 45 min. The scoured material and water were collected in a metal basin and allowed to settle for 12 h. After the clarified water was decanted, the settled solids were oven-dried at 105 °C to constant mass. The mean scouring mass loss was calculated, and unconfined compressive strength tests were performed on the scoured specimens.

2.3.5. Corrosion Resistance Test

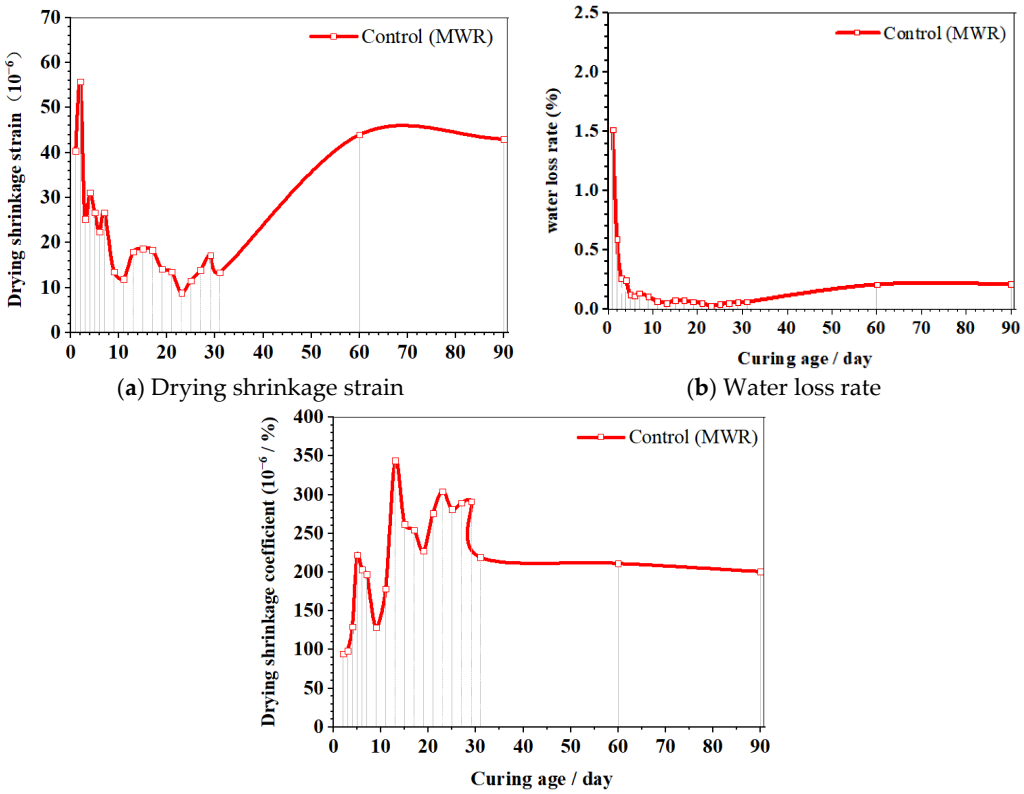
The sulfate attack resistance of waste rock aggregate cement-stabilized crushed stone was evaluated according to Method T 0582-2020 in JTG 3420-2020. Cylindrical specimens, 150 mm in diameter and 150 mm in height, were prepared according to Method T 0845 and cured for 28, 60, 90, and 180 days. A total of 16 groups were prepared, each containing three replicate specimens. The test matrix comprised specimens with and without the SK-D sulfate-resistant agent at each curing age and corresponding sulfate-solution and pure-water exposure groups. The agent dosage was 8% by mass of cement. A 5% sodium sulfate solution (50,000 ppm) was used as the aggressive medium, and corresponding reference specimens were exposed to pure water. The drying phase was conducted at 65 °C, the immersion period was 15 h, and each wet–dry cycle lasted 24 h. Upon reaching the designated curing age, specimens were subjected to 15 consecutive wet–dry cycles. Sulfate attack resistance was evaluated using mass loss and the unconfined compressive strength ratio, and the effect of the sulfate-resistant agent was assessed using these indices.

3. Results and Discussion

3.1. Drying Shrinkage Performance

3.1.1. Control Group

The control specimens of waste rock aggregate cement-stabilized crushed stone were prepared, cured, and tested for drying shrinkage according to Section 2.3.1. The drying shrinkage strain, water loss rate, and drying shrinkage coefficient at different ages are presented in Figure 9.



(**a**) Drying shrinkage strain (**b**) Water loss rate

(**c**) Drying shrinkage coefficient

Figure 9. Drying shrinkage test results of the control group.

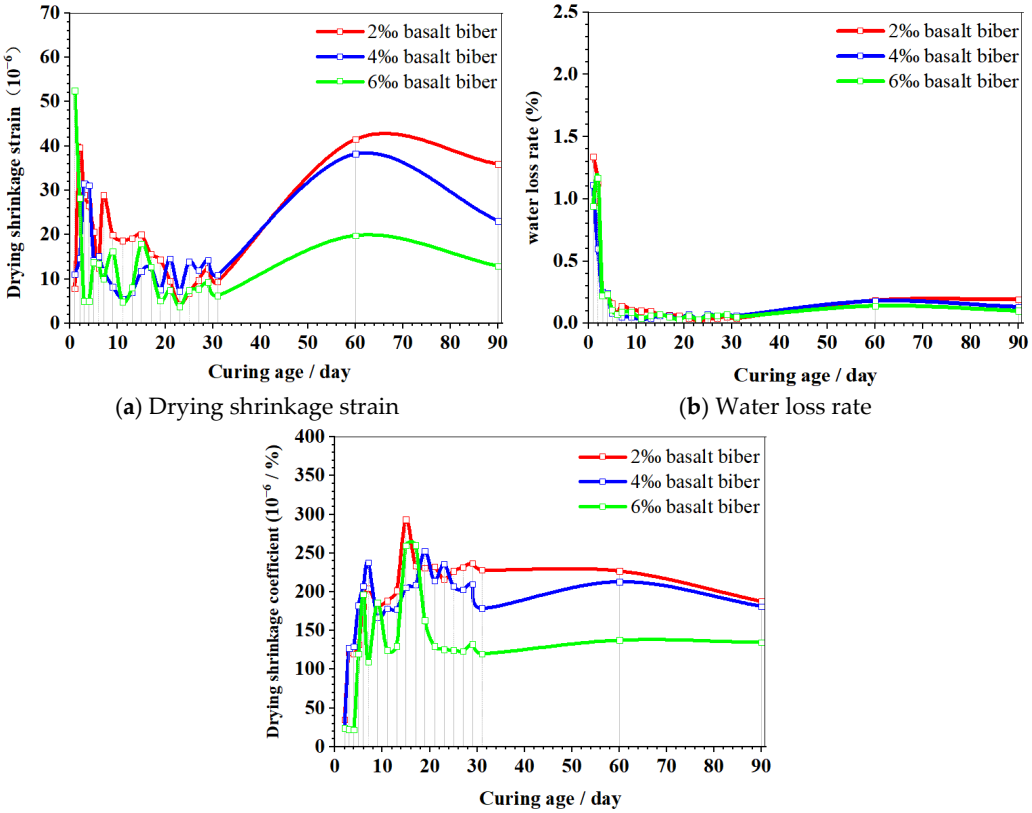
As shown in Figure 9a, the drying shrinkage strain decreased markedly at early ages, fluctuated at relatively low levels from 15 to 31 days, and increased again during the later period from 60 to 90 days. The strain was 40.33 × 10^{-6} on day 1 and decreased between days 3 and 7. From days 15 to 31, it ranged from 8.83 × 10^{-6} to 18.58 × 10^{-6}. A later increase was observed from days 60 to 90, with a minor peak at day 60. This behavior may be associated with long-term moisture migration and microstructural evolution within the cementitious matrix during continued hydration.

Figure 9b shows that the water loss rate was highest on day 1 (approximately 1.52%) and then decreased rapidly, remaining at a relatively low level of 0.03–0.21% after day 3. Most moisture loss therefore occurred during the early stage, while the evaporation rate slowed as the internal humidity gradually approached equilibrium with the surrounding environment.

As shown in Figure 9c, the drying shrinkage coefficient generally increased during the early and middle stages. A marked rise occurred after day 3, and the maximum was reached on day 13. Thereafter, despite fluctuations, the coefficient was mainly within 200 × 10^{-6}/% to 300 × 10^{-6}/%. This pattern indicates that deformation per unit water loss increased with age and may reflect increased internal restraint and potential microcrack development during drying.

3.1.2. Effect of Basalt Fiber

The drying shrinkage strain, water loss rate, and drying shrinkage coefficient of specimens containing different basalt fiber dosages are presented in Figure 10.



(**a**) Drying shrinkage strain (**b**) Water loss rate

(**c**) Drying shrinkage coefficient

Figure 10. Drying shrinkage behavior of waste rock aggregate cement-stabilized crushed stone with basalt fibers.

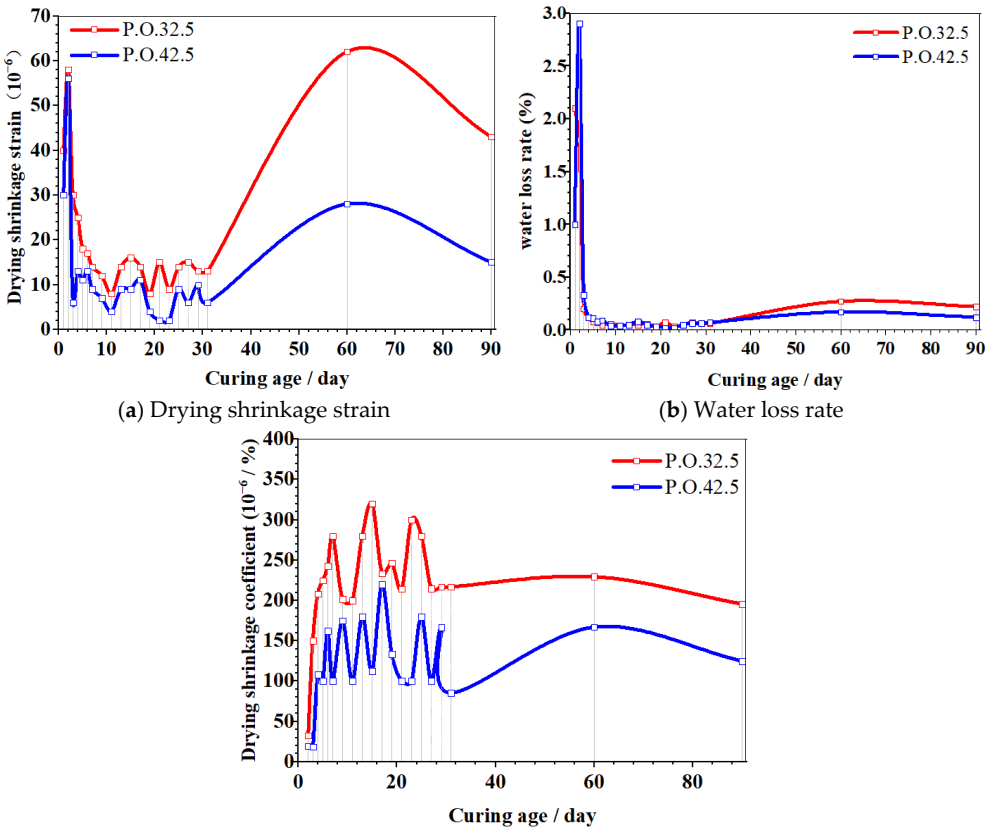
Compared with the control group, basalt fiber influenced the early-age drying shrinkage strain, as shown in Figure 10a. At fiber dosages of 2‰ and 4‰, the shrinkage strains at most ages were lower than those of the control, particularly on days 1, 7, and 21. At 6‰, the shrinkage strain fluctuated more markedly, and the day-1 strain was higher than that of the control, suggesting that a relatively high fiber content may increase initial heterogeneity and localized stress concentration. From days 60 to 90, the shrinkage strains of all fiber groups were lower than those of the control, indicating that basalt fiber can restrain long-term drying shrinkage to some extent.

As shown in Figure 10b, the water loss rates of the basalt fiber groups followed the same general pattern as the control: a high initial value followed by a rapid decrease. This indicates that basalt fiber had a limited influence on the overall moisture evaporation path. At several early ages, however, the water loss rates of some fiber groups were slightly lower than that of the control, which may be related to localized obstruction of moisture migration by the fibers.

Figure 10c shows that the drying shrinkage coefficients of the basalt fiber groups were generally lower than that of the control, particularly from approximately days 13 to 31. On day 13, the coefficient was $344.3 \times 10^{-6}/\%$ for the control group, whereas the values for the 2‰, 4‰, and 6‰ groups were $201.61 \times 10^{-6}/\%$, $177.71 \times 10^{-6}/\%$, and $129.92 \times 10^{-6}/\%$, respectively. These results indicate that fibers may reduce deformation per unit water loss through bridging and crack-arresting effects, thereby improving volumetric stability. These results suggest that fibers may reduce shrinkage deformation per unit water loss by restraining matrix deformation and crack development, thereby improving volumetric stability. Similar reductions in drying shrinkage have been reported for fiber-reinforced cement-stabilized macadam [36–38].

3.1.3. Effect of Low-Alkali Cement

The drying shrinkage strain, water loss rate, and drying shrinkage coefficient of specimens prepared with low-alkali cement are presented in Figure 11.



(**a**) Drying shrinkage strain (**b**) Water loss rate

(**c**) Drying shrinkage coefficient

Figure 11. Drying shrinkage behavior of waste rock aggregate cement-stabilized crushed stone incorporating low-alkali cement.

The early-age drying shrinkage strains of the low-alkali cement groups were generally lower than that of the control, indicating that low-alkali cement can reduce early shrinkage deformation. From days 60 to 90, the strain of the P.O. 32.5 group decreased from 62 $\times$ 10^{-6} to 43 $\times$ 10^{-6} but remained higher than that of the control. In contrast, the P.O. 42.5 group decreased from 28 $\times$ 10^{-6} to 15 $\times$ 10^{-6} and remained lower than the control, indicating relatively better control of long-term drying shrinkage under the investigated conditions.

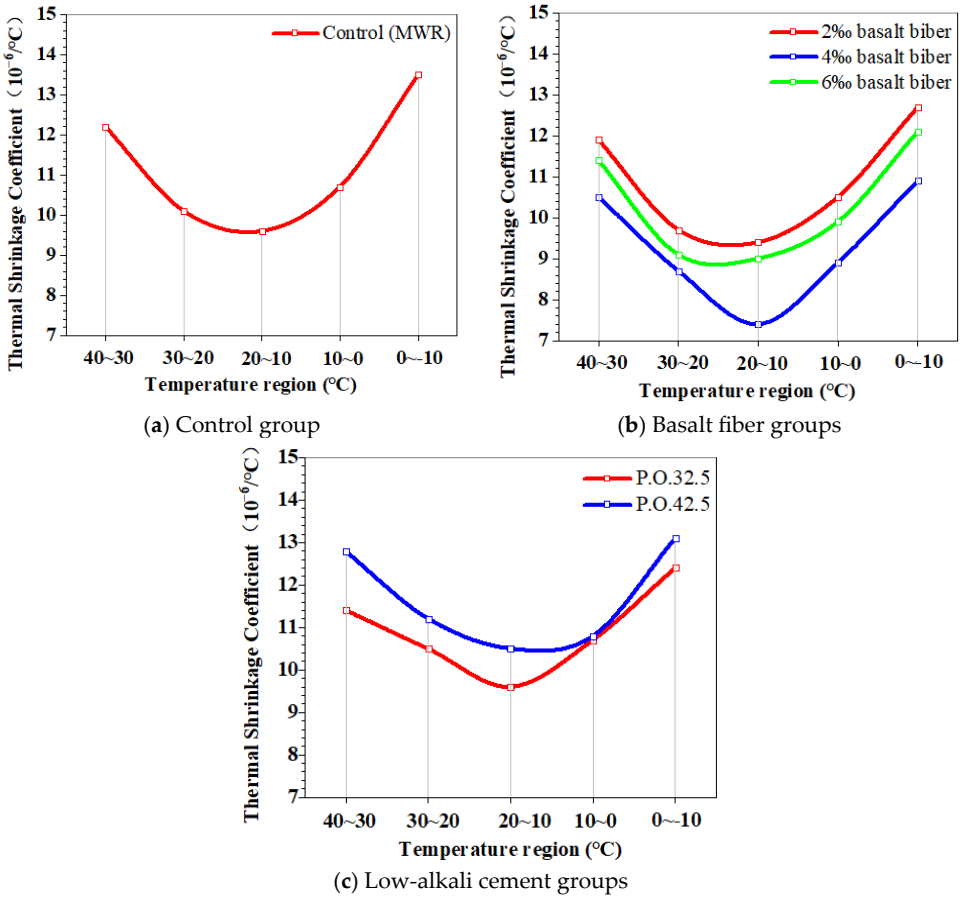
The water loss rates of both low-alkali cement groups followed the same general pattern as the control, with higher values at early ages followed by a rapid decrease, as shown in Figure 11b. The P.O. 42.5 group exhibited slightly lower water loss rates than the P.O. 32.5 and control groups at most ages, which may reflect slower moisture migration within its cementitious matrix.

The drying shrinkage coefficient of the P.O. 32.5 group was comparable to or higher than that of the control at several early ages, whereas the P.O. 42.5 group generally exhibited lower coefficients. Thus, the two low-alkali cements did not show a uniform response, and their effect depended on strength grade and age. Further interpretation should be made together with the complete technical data for the two low-alkali cements.

3.2. Thermal Shrinkage Performance

According to Section 2.3.2, waste rock aggregate cement-stabilized crushed stone specimens were prepared, cured, and tested for thermal shrinkage. The thermal shrinkage

coefficients of the different mixtures over each temperature interval are presented in Figure 12.



(**a**) Control group (**b**) Basalt fiber groups

(**c**) Low-alkali cement groups

Figure 12. Thermal shrinkage coefficient of different waste rock aggregate cement-stabilized crushed stone mixtures.

3.2.1. Control Group

As shown in Figure 12a, the thermal shrinkage coefficient of the control group initially decreased and subsequently increased as the temperature decreased from 40 °C to −10 °C. The inflection occurred in the 20–10 °C interval. From 40 °C to 10 °C, the coefficient decreased by 21.3%, indicating reduced contraction within the positive-temperature range. As the temperature decreased further from 10 °C to −10 °C, the coefficient increased and reached its maximum in the −10 °C interval. Because the specimens were oven-dried before testing, the increase at sub-zero temperatures is more reasonably associated with temperature-dependent deformation of the cementitious matrix and differential thermal deformation between the aggregate and cement paste than with freezing of pore water.

3.2.2. Effect of Basalt Fiber

As shown in Figure 12b, the thermal shrinkage coefficients of all basalt fiber groups were generally lower than or comparable to those of the control. With increasing fiber content, the coefficient initially decreased and then increased over most temperature intervals. The 4‰ group exhibited relatively favorable thermal shrinkage resistance among the investigated fiber contents, particularly from 20 °C to 10 °C, where its coefficient was 22.9% lower than that of the control group. This may be attributed to fiber bridging, which can partially restrain crack initiation and propagation within the cementitious matrix. Although the fiber-group coefficients increased in the 0 to −10 °C interval, they remained

lower than that of the control. The 6‰ group exhibited a higher coefficient than the 4‰ group, which may reflect increased difficulty in achieving uniform fiber dispersion at the higher dosage.

Overall, basalt fiber reduced the thermal shrinkage coefficient over most temperature intervals, with the 4‰ group showing relatively favorable behavior within the investigated range. Similar reductions in temperature shrinkage strain and coefficient have been reported for fiber-reinforced cement-stabilized macadam [37,38].

3.2.3. Effect of Low-Alkali Cement

Figure 12c presents the thermal shrinkage behavior of specimens incorporating P.O. 32.5 and P.O. 42.5 low-alkali cements. Their coefficients were generally slightly higher than or comparable to that of the control, showing no consistent improvement in reducing thermal shrinkage under the investigated conditions. The P.O. 32.5 group exhibited slightly lower coefficients than the P.O. 42.5 group over most intervals, while both groups showed relatively high coefficients in the 0 to −10 °C interval. These results indicate that replacing the reference cement with low-alkali cement did not provide a clear advantage in controlling thermal shrinkage. The differences may be related to hydration characteristics and pore-structure development, but verification would require further microstructural investigation.

3.3. Freeze–Thaw Resistance

Following Section 2.3.3, waste rock aggregate cement-stabilized crushed stone specimens were prepared, cured, and tested for freeze–thaw resistance. The unconfined compressive strengths before and after cycling and the freeze–thaw resistance coefficients are presented in Figures 13–15.

3.3.1. Control Group

As shown in Figure 13, the freeze–thaw resistance of the control group improved with increasing curing age. At 28 days, the freeze–thaw resistance coefficient was 0.73, corresponding to a 27% loss in unconfined compressive strength after five cycles. This may be associated with incomplete early-age hydration and relatively high internal porosity, which can increase susceptibility to damage caused by freezing and expansion of pore water. The black error bars in the figure represent the standard deviation of parallel specimen tests at each stage, and the same applies to the following figures. At 180 days, the coefficient increased to 0.89 and the strength loss decreased to 11%. Continued hydration and structural development during curing may therefore improve resistance to freeze–thaw cycling.

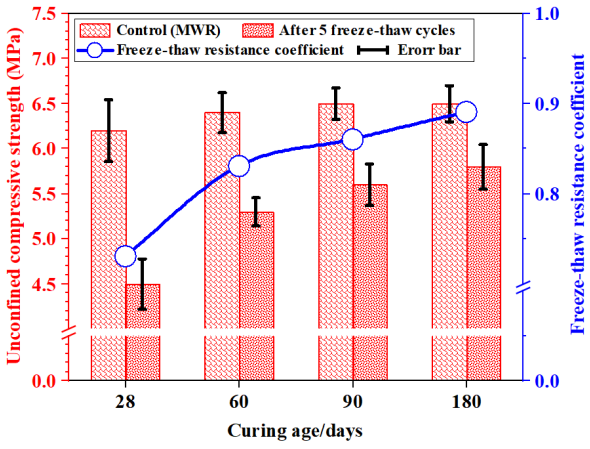
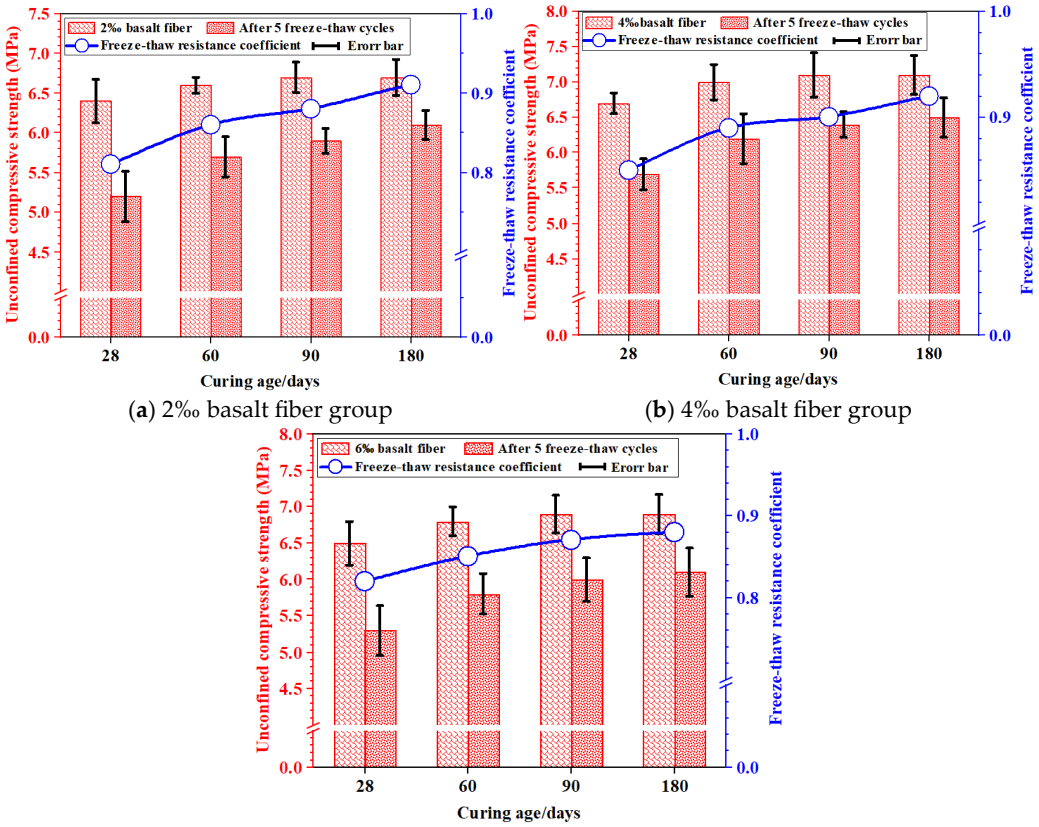


Figure 13. Freeze–thaw resistance of the control group at different curing ages.

3.3.2. Effect of Basalt Fiber

Figure 14 shows that basalt fiber improved freeze–thaw resistance, with the 4‰ dosage exhibiting relatively better performance among the investigated fiber contents. The results indicate that an appropriate basalt fiber dosage can improve the freeze–thaw resistance of waste rock aggregate cement-stabilized crushed stone.



(**a**) 2‰ basalt fiber group (**b**) 4‰ basalt fiber group

(**c**) 6‰ basalt fiber group

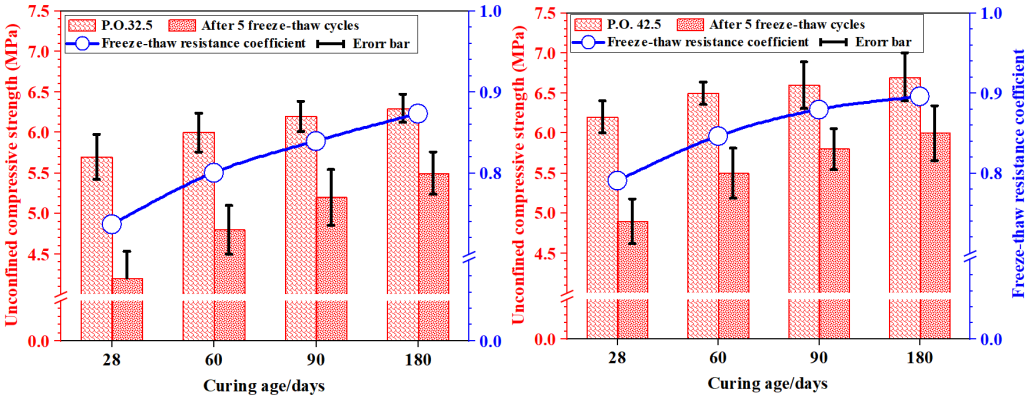
Figure 14. Freeze–thaw resistance of the basalt fiber groups at different curing ages.

At all curing ages, the unconfined compressive strengths of the fiber-reinforced specimens before and after freeze–thaw cycling were generally higher than those of the control. The response depended on fiber dosage. The 4‰ group achieved a freeze–thaw resistance coefficient of 0.85 at 28 days and 0.92 at 180 days. Within the investigated range, this dosage may provide a relatively suitable balance between fiber dispersion and bridging effects. The 6‰ group exhibited a slightly lower coefficient, indicating that a higher fiber content may increase the difficulty of uniform dispersion and potentially cause local agglomeration. These findings are consistent with previous studies reporting progressive strength and modulus degradation together with the development of microcracks and internal defects in cement-stabilized crushed stone under freeze–thaw cycling [2]. Coupling freeze–thaw action with repeated wheel loading can further accelerate structural deterioration and deformation [39].

3.3.3. Effect of Low-Alkali Cement

The P.O. 32.5 and P.O. 42.5 low-alkali cement groups exhibited slightly lower freeze–thaw resistance than the control under the investigated conditions, as shown in Figure 15. This was especially evident for the P.O. 32.5 group, whose unconfined compressive strength before cycling was 5.7 MPa at 28 days. Its post-cycle strength was correspondingly lower than that of the control, and the larger absolute strength loss may also be associated with

the lower cement strength grade. The freeze–thaw resistance coefficients of both low-alkali cement groups increased with curing age, indicating continued hydration and structural development.



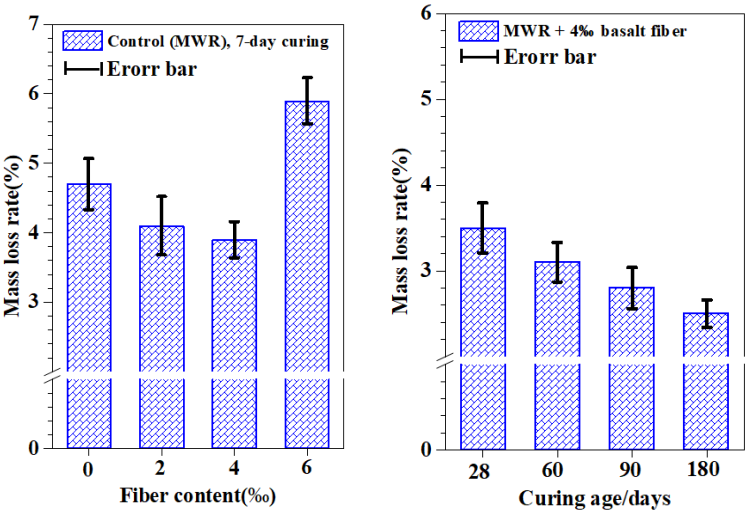
(**a**) P.O. 32.5 low-alkali cement group (**b**) P.O. 42.5 low-alkali cement group

Figure 15. Freeze–thaw resistance of the low-alkali cement groups at different curing ages.

However, the improvement with curing age was limited. This may be related to similarities in hydration behavior and pore-structure development between the low-alkali and reference cements, resulting in no consistent enhancement of freeze–thaw resistance.

3.4. Scouring Resistance

The waste rock aggregate cement-stabilized crushed stone specimens were prepared, cured, and tested according to Section 2.3.4. The scouring mass loss rates of mixtures containing different basalt fiber contents after 7 days of standard curing are shown in Figure 16a.



(**a**) Different fiber contents (**b**) Different curing periods

Figure 16. Scouring resistance test results of waste rock aggregate cement-stabilized crushed stone.

After 7 days of curing, the 2‰ and 4‰ basalt fiber groups exhibited scouring mass loss rates of 4.1% and 3.9%, corresponding to reductions of 12.8% and 17.0% relative to the control, respectively. At 6‰, the mass loss increased and did not show a comparable improvement. This may be related to the greater difficulty of achieving uniform fiber dispersion at the higher dosage, which could affect mixture homogeneity. Therefore, the 4‰ dosage was selected for the subsequent curing-age study shown in Figure 16b.

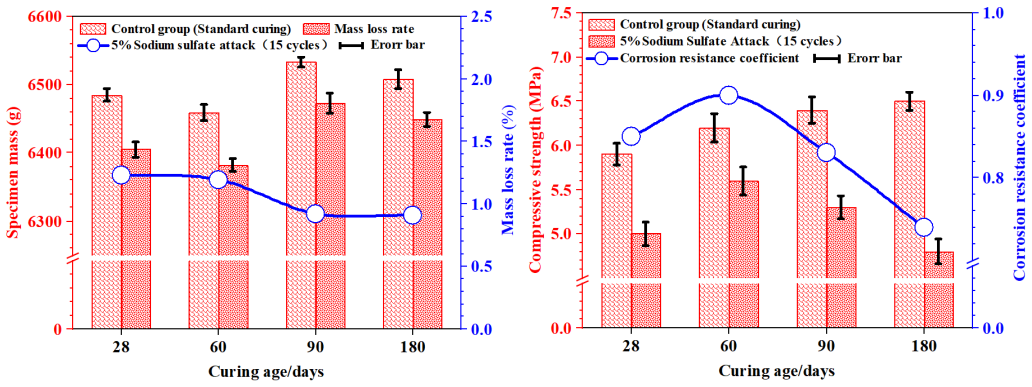
For the 4‰ fiber group, the scouring mass loss rate decreased continuously as the curing age increased from 28 to 180 days. The loss rate was 3.5% at 28 days and then decreased steadily. This trend may be associated with continued cement hydration and gradual development of the internal structure, which can improve the integrity of the cementitious matrix and its resistance to surface particle detachment. Previous dynamic-water scouring tests have related scouring resistance to compressive strength, cementitious bonding, aggregate-skeleton stability, and the development of internal cracks and pores [35].

It should be noted that the present scouring test focused on mechanical degradation under hydraulic action. The potential release of heavy metals, sulfate ions, or other chemical components during prolonged water exposure was not evaluated in this manuscript and requires separate investigation.

3.5. Corrosion Resistance

3.5.1. Effect of Low-Alkali Cement

According to Section 2.3.5, control specimens of waste rock aggregate cement-stabilized crushed stone without the sulfate-resistant agent were prepared and cured. The sulfate attack resistance results are presented in Figure 17.



(**a**) Mass loss rate (**b**) Corrosion resistance coefficient

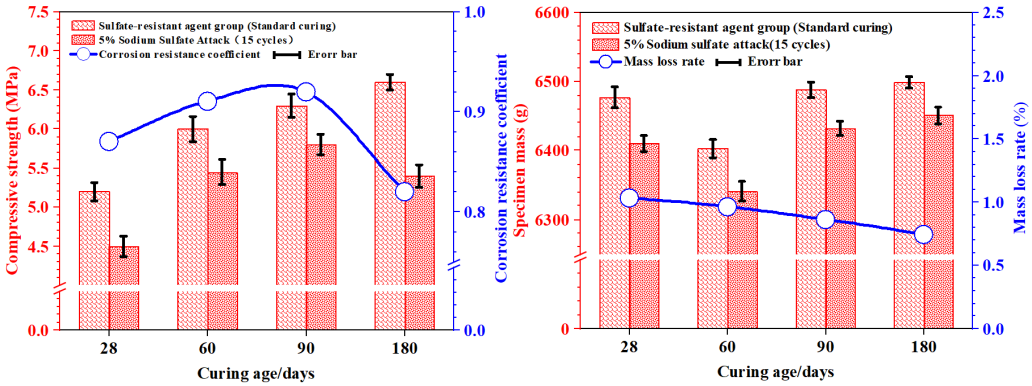
Figure 17. Sulfate attack resistance test results of the control group.

As shown in Figure 17a, the mass loss rate after 15 wet–dry cycles in 5% sodium sulfate solution generally decreased with increasing curing age. It decreased slightly from 1.23% at 28 days to 1.19% at 60 days and then to 0.92% at 90 days, after which it remained relatively stable up to 180 days. This indicates that specimens cured for longer periods experienced lower material loss under the adopted exposure conditions. The reduction may be associated with continued development of the cementitious matrix, which can reduce surface spalling and dissolution during wet–dry cycling.

As shown in Figure 17b, the corrosion resistance coefficient did not follow the same monotonic trend as the mass loss rate. It increased slightly from 28 to 60 days and then decreased at 90 and 180 days, reaching its lowest value at 180 days. Thus, although prolonged curing reduced visible mass loss, it did not completely prevent strength degradation after sulfate exposure. The later decrease may be associated with accumulated internal damage during wet–dry cycling; confirmation of the deterioration mechanism would require microstructural investigation.

3.5.2. The Effect of the Sulfate-Resistant Agent

The sulfate attack resistance of specimens containing 8% sulfate-resistant agent by mass of cement was evaluated at the same curing ages. The results are presented in Figure 18.



(**a**) Corrosion resistance coefficient (**b**) Mass loss rate

Figure 18. Sulfate attack resistance test results of specimens incorporating the sulfate-resistant agent.

As shown in Figure 18b, the mass loss rate of the agent-modified specimens generally decreased with increasing curing age after 15 wet–dry cycles in 5% sodium sulfate solution. At all investigated ages, the values were lower than those of the corresponding control specimens. At 28 days, the mass loss rate was approximately 16.3% lower than that of the control, and the lowest value of 0.74% was recorded at 180 days. These results indicate that the sulfate-resistant agent reduced material loss under the exposure conditions adopted in this study.

As shown in Figure 18a, the corrosion resistance coefficient initially increased and subsequently decreased with curing age. It reached 0.92 at 90 days, compared with 0.83 for the corresponding control group. Although it decreased at 180 days, it remained higher than that of the control at the same age. The sulfate-resistant agent therefore improved strength retention under the investigated conditions, particularly at 90 days, while the later decrease suggests that its protective effect may attenuate as sulfate-related damage accumulates.

Overall, specimens containing the sulfate-resistant agent exhibited lower mass loss rates and higher corrosion resistance coefficients than the control specimens under the investigated conditions. Previous research has shown that salt exposure can produce either mass loss or mass gain depending on the salt type while still reducing mechanical strength, indicating that mass variation and strength degradation may follow different trends. Vibrational action can additionally accelerate Ca^{2+} leaching and dissolution damage in cement-stabilized macadam [26].

The sulfate attack assessment was limited to 15 wet–dry cycles. Consequently, the results primarily reflect the comparative resistance of the investigated mixtures under the specified laboratory conditions and should not be interpreted as direct evidence of long-term field durability. Additional exposure cycles, coupled environmental actions, and field validation are required before long-term engineering recommendations can be established.

4. Conclusions

This study investigated the cracking resistance and durability of cement-stabilized crushed stone incorporating 50% lead–zinc mine waste rock aggregate and evaluated the effects of basalt fiber, low-alkali cement, and a sulfate-resistant agent. Based on the investigated laboratory conditions, the following conclusions were obtained:

(1) Basalt fiber reduced the drying shrinkage strain and thermal shrinkage coefficient of waste rock aggregate cement-stabilized crushed stone. Among the investigated fiber contents, the 4‰ group exhibited relatively favorable shrinkage resistance. In contrast, low-alkali cement showed limited effectiveness in reducing thermal shrinkage.

(2) Freeze–thaw resistance generally improved with increasing curing age. The specimens containing 4‰ basalt fiber exhibited relatively better freeze–thaw resistance among the investigated fiber contents, whereas low-alkali cement did not provide a consistent improvement.

(3) The incorporation of 2‰ and 4‰ basalt fiber reduced scouring mass loss after 7 days of curing, while the 6‰ fiber content did not produce a comparable improvement. For specimens containing 4‰ basalt fiber, the scouring mass loss decreased with increasing curing age.

(4) Under 15 wet–dry cycles in a 5% sodium sulfate solution, the sulfate-resistant agent reduced mass loss and improved strength retention compared with the control group. However, the corrosion resistance coefficient decreased at 180 days, indicating that the protective effect may attenuate with continued sulfate exposure.

Overall, the results support the feasibility of using lead–zinc mine waste rock as a partial coarse aggregate replacement in cement-stabilized crushed stone under the investigated laboratory conditions. Further studies involving additional sulfate exposure cycles, chemical leaching evaluation, coupled environmental actions, and field validation are required before long-term engineering recommendations can be established. The environmental stability and heavy metal release potential of the waste rock material used in this study will be investigated in the continuation of this study.

Author Contributions: Conceptualization, Z.Z. and X.L.; methodology, Y.H. and X.L.; validation, J.M. and J.Y.; investigation, Y.H., C.S. and L.Z.; resources, Y.H. and X.L.; data curation, J.M. and J.Y.; writing—original draft preparation, Y.H., C.S., and L.Z.; writing—review and editing, Z.Z., and X.L.; supervision, X.L. and Z.Z.; project administration, Y.H. and C.S.; funding acquisition, X.L. and Z.Z. All authors have read and agreed to the published version of the manuscript.

Funding: The authors gratefully acknowledge the financial support provided by Yunnan Fundamental Research Projects (grant No. 202301AU070065, No. 202501AT070036), Yunnan Provincial Department of Transportation Technology Innovation and Demonstration Project (grant No. 2022-73), Yunnan Innovation Team of Vehicle-Road Cooperative Control and Operation Safety (Grant No. 202505AS350024), and the 2025 Graduate Top Innovative Talent Program of Kunming University of Science and Technology (No. CA26005M064A).

Institutional Review Board Statement: Not applicable.

Informed Consent Statement: Not applicable.

Data Availability Statement: The data that support the findings of this study are available from the corresponding author upon reasonable request.

Conflicts of Interest: Authors Yinglong Hu, Chenghai Sun and Lizhou Zhao were employed by the company Yunnan Yunlan Expressway Investment and Development Co., Ltd. Authors Jian Miao and Jinggang Yin were employed by the company YCIH Road Surface Engineering Co., Ltd. The remaining authors declare that the research was conducted in the absence of any commercial or financial rela-tionships that could be construed as a potential conflict of interest.

References

1. Zhen, S. Study on Durability Improvement Technology of Cement Stabilized Macadam Base Material. Master's Thesis, Changsha University of Science & Technology, Changsha, China, 2019.
2. Xiao, R.; An, B.; Wu, F.; Wang, W.; Sui, Y.; Wang, Y. Freeze-Thaw Damage Characterization of Cement-Stabilized Crushed Stone Base with Skeleton Dense Gradation. *Materials* **2024**, *17*, 1228. [CrossRef] [PubMed]
3. Qian, G.; Huang, T.; Bai, S. Use of Cement-Stabilized Granite Mill Tailings as Pavement Subbase. *J. Mater. Civ. Eng.* **2011**, *23*, 8–15. [CrossRef]
4. Liu, J. Research on the Application of Tailings in Highway Base. Master's Thesis, North China University of Science and Technology, Tangshan, China, 2023.

5. Ren, Q.; Bu, F.; Huang, Q.; Yin, H.; Zhu, Y.; Ma, R.; Ding, Y.; Zhang, L.; Li, J.; Ju, L.; et al. Effect of Iron Ore Tailings Replacing Porous Basalt on Properties of Cement Stabilized Macadam. *Korean J. Mater. Res.* **2024**, *34*, 291–302. [CrossRef]
6. El Berdai, Y.; Trauchessec, R.; Taha, Y.; Safhi, A.E.M.; Hakkou, R.; Benzaazoua, M. Assessing the Suitability of Phosphate Waste Rock as a Construction Aggregate. *Buildings* **2024**, *14*, 2375. [CrossRef]
7. Chlahbi, S.; Elghali, A.; Inabi, O.; Belem, T.; Zerouali, E.; Benzaazoua, M. Integrated approach to sustainable utilization of phosphate waste rock in road embankments: Experimental insights, stability analysis, and preliminary economic evaluation. *Case Stud. Constr. Mater.* **2024**, *20*, e03222. [CrossRef]
8. Beniddar, H.; El Machi, A.; El Abbassi, F.E.; Taha, Y.; Benzaazoua, M.; Hakkou, R. Sustainable utilization of phosphate mine waste rocks as sand substitutes in cement mortar production. *Constr. Build. Mater.* **2024**, *438*, 136949. [CrossRef]
9. Benahsina, A.; El Haloui, Y.; Taha, Y.; Elomari, M.; Bennouna, M.A. Natural sand substitution by copper mine waste rocks for concrete manufacturing. *J. Build. Eng.* **2022**, *47*, 103817. [CrossRef]
10. Inabi, O.; Khalil, A.; Zouine, A.; Hakkou, R.; Benzaazoua, M.; Taha, Y. Investigation of the innovative combined reuse of phosphate mine waste rock and phosphate washing sludge to produce eco-friendly bricks. *Buildings* **2024**, *14*, 2600. [CrossRef]
11. Sbi, S.; Aboulayt, A.; Borja, W.; Mansouri, S.; Idrissi, H.E.B.E.; Samih, Y.; Semlal, N.; Hannache, H.; Tamraoui, Y.; Alami, J. An advance understanding of the alkali activation of cover layers waste rocks from phosphate mines: Mechanical, structure and microstructure studies. *Constr. Build. Mater.* **2022**, *346*, 128472. [CrossRef]
12. Rai, A.; Rao, D.B.N. Utilisation potentials of industrial/mining rejects and tailings as building materials. *Manag. Environ. Qual. Int. J.* **2005**, *16*, 605–614. [CrossRef]
13. Liu, J. Fundamental Research on the High Performance Concrete Made by Iron Tailings and Iron Barren Rocks. Ph.D. Thesis, University of Science and Technology Beijing, Beijing, China, 2014.
14. Vyshar, O.; Stolboushkin, A.; Rakhimova, G.; Stanevich, V.; Rakhimov, M. Study of the properties of overburdened rocks from coal mining: Overburden–as a raw material in the production of ceramic bricks. *Geomate J.* **2023**, *25*, 86–94. [CrossRef]
15. Zhang, J.; Zou, Q.; Cai, W.; Zhang, L.; Ge, H.; Li, H. Mechanical properties and energy evolution of cemented tailings-rock powder backfill under uniaxial compression: Effect of rock powder type and content. *Sci. Rep.* **2026**, *16*, 5855. [CrossRef] [PubMed]
16. Hui, C.; Aiai, W.; Lianku, X.; Xi-Zhi, Z.; Yong-Ding, W.; Qian, G. Research progress of solid waste resource utilization backfill mining for Jinchuan Nickel Mine, China. *Front. Mater.* **2024**, *11*, 1442564. [CrossRef]
17. Yang, C.; Yuan, H.; An, G. Comprehensive utilization of waste rock and tailings in Kangjiawan lead zinc mine. *World Nonferrous Met.* **2020**, *11*, 152–154.
18. Ally, A.N.; Blanche, M.M.; Nana, U.J.M.P.; Grâce, M.M.; Zang, É.R.; François, N.; Pettang, C. Potential use of coltan mining waste rock in road construction. *Adv. Civ. Archit. Eng.* **2023**, *14*, 14–31. [CrossRef]
19. Ghanizadeh, A.R.; Safi Jahanshahi, F. A case study on potential use of stabilized mine overburden wastes as pavement materials. *Transp. Infrastruct. Geotechnol.* **2024**, *11*, 865–899. [CrossRef]
20. Wen, P.; Wang, C.; Gao, X.; Chen, M.; Chai, Z. Effect of environmental factors on mechanical properties and damage characteristics of mine overburden used in subgrade. *Int. J. Pavement Eng.* **2023**, *24*, 2032698. [CrossRef]
21. Shi, Z.; Xue, Q. Progress on Domestic Investigation of Building Materials Conversion from Lead-Zinc Tailing. *Bull. Chin. Ceram. Soc.* **2018**, *37*, 508–512.
22. Zhao, L. Study on the Preparation of Fine Calcium Carbonate from a Lead-Zinc Tailings in Yunnan. Master's Thesis, Central South University, Changsha, China, 2023.
23. Chen, H. Resource Utilization of Solid Wastes from Industry and Mining Industry in the Building Materials Field. *IOP Conf. Ser. Earth Environ. Sci.* **2019**, *310*, 022023. [CrossRef]
24. Çullu, M. Kurşun-çinko maden artığı kayaçlarla üretilen betonların mekanik ve fiziksel özelliklerinin araştırılması. *Politek. Derg.* **2018**, *21*, 427–435. [CrossRef]
25. Congcong, Y.; Guanghui, X.; Zhengqi, G. Research on substitution of the waste rock in lead-zinc mines for dolomite in iron ore sintering process. *Sinter. Pelletizing* **2023**, *48*, 63–69.
26. Wang, C.; Chen, Y.; An, B.; Guo, Q.; Wang, Y. Impact of salt erosion on mechanical and drying shrinkage performance of cement-stabilized macadam. *Front. Mater.* **2024**, *11*, 1453768. [CrossRef]
27. National Development and Reform Commission. *Industrial Structure Adjustment Guidance Catalogue (2024 Edition)*; NDRC: Beijing, China, 2024.
28. *JTG 3432—2024*; Test Methods of Aggregate for Highway Engineering. China Communications Press: Beijing, China, 2024.
29. *JTG F40-2004*; Technical Specifications for Construction of Highway Asphalt Pavements. China Communications Press: Beijing, China, 2004.
30. *JTG 3420—2020*; Testing Methods of Cement and Concrete for Highway Engineering. China Communications Press: Beijing, China, 2020.
31. *GB 175-2023*; Common Portland Cement. Standards Press of China: Beijing, China, 2023.

32. *JTG/T F20-2015*; Technical Guidelines for Construction of Highway Roadbases. China Communications Press: Beijing, China, 2015.
33. Quan, L.; Liu, J.; He, Z.; Li, L. Study on the Road Performance of Cement Stabilised Gravel with Emulsified Asphalt Pre-Weakened Aggregate-Mortar Interface. *Civ. Eng.* **2024**, *13*, 2406–2417.
34. *JTG 3441—2024*; Test Methods of Materials Stabilized with Inorganic Binders for Highway Engineering. China Communications Press: Beijing, China, 2024.
35. Yu, H.; Zhao, Q.; Zhang, C.; Feng, B. Experimental Study of Dynamic Water Erosion to Cement-Stabilized Macadam Base. *Highway* **2019**, *64*, 18–26.
36. Tan, S.; Wang, C.; Zheng, Q.; Chen, F.; Huang, Y. Durability performance of PVA fiber cement-stabilized macadam. *Sustainability* **2022**, *14*, 16953. [CrossRef]
37. Wu, D. Study on Crack Resistance of Basalt and Polyvinyl Alcohol Hybrid Fiber Semi-Rigid Base. Master's Thesis, Chang'an University, Xi'an, China, 2023.
38. He, Y. Study on Mechanical Properties and Cracking Resistance of Cement-Stabilized Macadam Mixed with Polyvinyl Alcohol (PVA) Fiber. Master's Thesis, Chongqing Jiaotong University, Chongqing, China, 2016.
39. Wang, Y.; Tan, Y.; Guo, M.; Wang, X. Mechanical response and damage evaluation of cement-stabilized crushed stone base roads under load and freeze–thaw coupling effects. *Constr. Build. Mater.* **2025**, *458*, 139741. [CrossRef]

Disclaimer/Publisher's Note: The statements, opinions and data contained in all publications are solely those of the individual author(s) and contributor(s) and not of MDPI and/or the editor(s). MDPI and/or the editor(s) disclaim responsibility for any injury to people or property resulting from any ideas, methods, instructions or products referred to in the content.